Biosensors and Bioelectronics 208 (2022) 114201

Contents lists available at ScienceDirect

Biosensors and Bioelectronics

journal homepage: www.elsevier.com/locate/bios

Fourier light-field imaging of human organoids with a hybrid point-spread function

Wenhao Liu [a], Ge-Ah R Kim [b], Shuichi Takayama [a,c], Shu Jia [a,c,*]

[a] Wallace H. Coulter Department of Biomedical Engineering, Georgia Institute of Technology and Emory University, Atlanta, GA, 30332, USA
[b] School of Materials Science and Engineering, Georgia Institute of Technology, Atlanta, GA, 30332, USA
[c] Parker H. Petit Institute for Bioengineering and Bioscience, Georgia Institute of Technology, Atlanta, GA, 30332, USA

ARTICLE INFO

Keywords:
Human organoids
Light-field microscopy
3D imaging
Point-spread function
Extracellular physical cues

ABSTRACT

Volumetric interrogation of the cellular morphology and dynamic processes of organoid systems with a high spatiotemporal resolution provides critical insights for understanding organogenesis, tissue homeostasis, and organ function. Fluorescence microscopy has emerged as one of the most vital and informative driving forces for probing the cellular complexity in organoid research. However, the underlying scanning mechanism of conventional imaging methods inevitably compromises the time resolution of volumetric acquisition, leading to increased photodamage and inability to capture fast cellular and tissue dynamic processes. Here, we report Fourier light-field microscopy using a hybrid point-spread function (*hPSF*-FLFM) for fast, volumetric, and high-resolution imaging of entire organoids. *hPSF*-FLFM transforms conventional 3D microscopy and enables exploration of less accessible spatiotemporally-challenging regimes for organoid research. To validate *hPSF*-FLFM, we demonstrate 3D imaging of rapid responses to extracellular physical cues such as osmotic and mechanical stresses on human induced pluripotent stem cells-derived colon organoids (hCOs). The system offers cellular (2–3 μm and 5–6 μm in *x*-*y* and *z*, respectively) and millisecond-scale spatiotemporal characterization of whole-organoid dynamic changes that span large imaging volumes (>900 μm × 900 μm × 200 μm in *x*, *y*, *z*, respectively). The *hPSF*-FLFM method provides a promising avenue to explore spatiotemporal-challenging cellular responses in a wide variety of organoid research.

1. Introduction

Organoids are stem cell-derived 3D multicellular *in vitro* tissue constructs that recapitulate the pertinent *in vivo* organs (Osakada et al., 2009; Sato et al., 2009). These miniaturized and simplified model systems have a remarkable resemblance to the microscale tissue architectures and key functionalities of their *in vivo* counterparts, overcoming the barriers of classical cell line and animal model systems to understanding human biology and medicine (Kim et al., 2020; Lancaster and Knoblich, 2014; Rossi et al., 2018). The recent advances of various organoid systems have demonstrated their great potential and promise in modeling tissue development and disease (Clevers, 2016; Mu and Zhang, 2022), high scalability and amenability to biomaterials and protocols (Kratochvil et al., 2019), and in a wide range of applications in basic biology (Drost and Clevers, 2018), drug discovery (Broutier et al., 2017; Ching et al., 2021; Weeber et al., 2017), and regenerative medicine (Grassi et al., 2019).

Essentially, thorough exploitation of the promises of organoids requires a detailed picture of the cellular complexity modeled with organoids. Indeed, fluorescence microscopy has become a major driving force to probe this complexity—to reveal the phenotypic and functional states of organoid development and pathogenesis, gaining us critical insights relevant to their original organs (Rios and Clevers, 2018). Unlike traditional tissue sectioning, organoids are generated in 3D matrices and thereby necessitate live, noninvasive observation to study fine cellular details within an intact tissue architecture *in vitro*. To address this need, one major consideration underlying live imaging of organoids lies in the balance between volumetric capability (e.g., the spatiotemporal resolution, signal-to-noise ratio (SNR), optical sectioning) and sample health (e.g., phototoxicity, photobleaching) (Laissue et al., 2017). Conventional wide-field systems, for instance, have difficulty to visualize 3D cultures with more than 2–3 cell layers due to the lack of optical sectioning. Major 3D fluorescence microscopy techniques such as confocal, multiphoton, and light-sheet fluorescence microscopy have

* Corresponding author.
E-mail address: shu.jia@gatech.edu (S. Jia).

https://doi.org/10.1016/j.bios.2022.114201
Received 7 January 2022; Received in revised form 25 February 2022; Accepted 17 March 2022
Available online 26 March 2022

thus far substantially transformed the study of complex 3D structures and processes of organoids at the cellular and subcellular levels (Bolhaqueiro et al., 2019; Dekkers et al., 2019; Drost et al., 2015; Rakotoson et al., 2019; Serra et al., 2019). All these techniques have contributed to elegant 3D characterizations of fixed and cleared intact organoids (Almagro et al., 2021; Dekkers et al., 2019). However, though confocal or multiphoton laser scanning techniques offer a high 3D resolution, they are time-consuming and may lead to increased photodamage, making the strategies less optimum for live imaging of large organoid samples (Rios and Clevers, 2018). By contrast, light-sheet microscopy provides effective optical sectioning without significant photobleaching and altered physiology of organoid specimens, thus becoming a valuable tool for the long-term investigation of live organoids (Alladin et al., 2020; Hof et al., 2021; Serra et al., 2019). However, the light-sheet methods remain suboptimal in broad applicability, primarily due to the inadequate volumetric image throughput (Reynaud et al., 2015). Specifically, the underlying light-sheet scanning mechanism, augmented by potential tile stitching, inevitably entails a compromised volume time resolution, especially when capturing complete or multiple organoids ranging over hundreds of micrometers, leading to an unmet imaging gap for organoid study to capture fast cellular and tissue dynamic processes in a simultaneous, volumetric manner (e.g., collective cellular responses at sub-second time scales across whole organoids).

The development of light-field microscopy (LFM) techniques suggests a promising solution to organoid imaging. In principle, LFM can simultaneously capture both the 2D spatial and 2D angular information of light, permitting computational retrieval of the volume of a biological sample from a single camera frame (Broxton et al., 2013; Fan et al., 2019; Javidi et al., 2020; Levoy et al. 2006, 2009; Li et al., 2019; Nobauer et al., 2017; Pégard et al., 2016; Prevedel et al., 2014; Wagner et al., 2019; Wu et al., 2021). Furthermore, the recent advances into Fourier LFM (FLFM, or extended LFM—XLFM) have overcome the intrinsic uneven sampling of the optical signals in LFM, achieving substantially enhanced volume image quality and computational efficiency (Cong et al., 2017; Guo et al., 2019; Llavador et al., 2016; Scrofani et al., 2018). The advancement has revolutionized the volumetric study of various biological samples at cellular to subcellular, milliseconds spatiotemporal resolution, ranging from the functional brain (Cong et al., 2017; Yoon et al., 2020; Zhang et al., 2021) to single-cell specimens (Hua et al., 2021; Sims et al., 2020). Therefore, despite remaining unexplored, the Fourier light-field methodology promises fast snapshot and scanning-free recording of intact organoids and their dynamic cellular processes with minimum photodamage per volumetric acquisition compared to existing techniques.

In practice, however, such a Fourier light-field system demands two major considerations to transform conventional schemes suitable for organoid study. *First*, organoid model systems present a wide morphological and functional variability and thus require flexible configurations to obtain cellular details at versatile spatiotemporal scales. Here, we provide detailed design modeling and protocol and corresponding instrumental strategies for constructing the microscope so that the approach can be readily adjustable to a wide range of organoids of various dynamics, sizes and shapes. *Second*, existing Fourier light-field tissue imaging methods rely on numerical or experimental point-spread functions (PSFs) to retrieve volumetric information (Cong et al., 2017; Guo et al., 2019). They have offered adequate reconstruction precision and final image quality of tissues in two main scenarios. Numerical PSFs provide faithful simulation for imaging systems using standard optical elements (e.g., commercial microscope frame, mass-produced microlens arrays) as opposed to custom-built systems

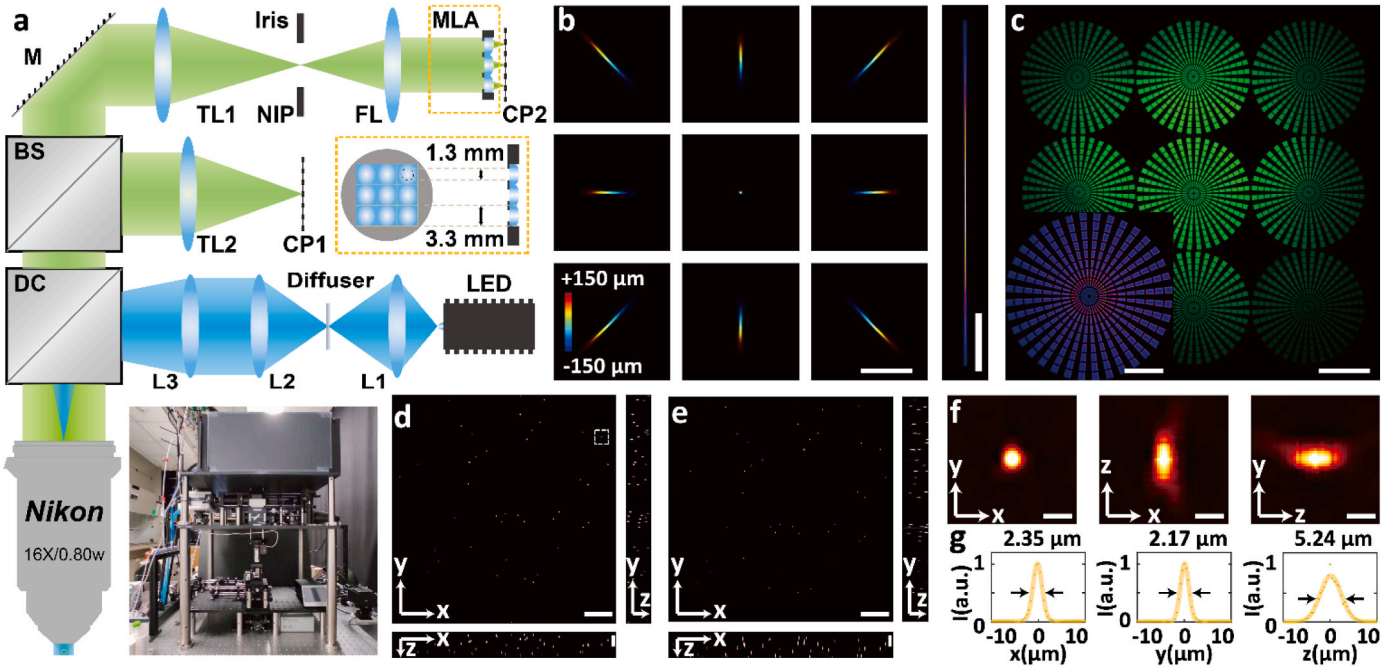

Fig. 1. Fourier light-field microscopy with a hybrid point-spread function (*hPSF*-FLFM). a Schematic of the experimental setup. LED, light-emitting diode; BS, beam splitter; DC, dichroic cube; M, mirror; TL, tube lens; NIP, native image plane; FL, Fourier lens; CP, camera plane; MLA, microlens array. Top inset displays the 3 × 3 MLA with the pitch $d_1 = 3.30$ mm and aperture $d_{MLA} = 1.30$ mm. Bottom inset shows a photo of the custom-built system (detailed in Supplementary Note 1). b Axial stack projection (step size = 400 nm) of the hybrid point-spread function (hPSF) through the 3 × 3 microlenses within an axial range from -150 μm to 150 μm, as color-coded in the color scale bar. The inset exhibits the in-depth view of the PSF element of the central microlens. c Raw light-field image of a fluorescent sector star (physical diameter = 893 μm) and the corresponding synthesized focal image (inset). d 3D reconstructed light-field images in *x-y*, *x-z*, *y-z* views of 2-μm fluorescent beads distributed in 3D agarose gel of ~ 900 μm × 900 μm × 90 μm e Wide-field images of the same volume, acquired by overlaying 91 axial stacks at a step size of 1 μm, showing consistent sample structure while less compact axial profiles at each depth. f,g Zoomed-in *x-y*, *x-z*, *y-z* images (f) of the boxed region in d and their corresponding cross-sectional profiles (g), exhibiting the FWHM values of 2.35 μm in *x*, 2.17 μm in *y*, and 5.24 μm in *z*. Scale bars: 100 μm (b), 400 μm (c), 200 μm (c inset), 100 μm (d,e), 40 μm (d,e insets), 10 μm (f).

and parts, which may exhibit various alignment deviations in practice. In contrast, experimental PSFs have been demonstrated for accurate recording of neural activities that exhibit sufficient spatiotemporal sparsity. At the same time, fluorescence fluctuations and a low SNR in increased depths may cause reconstruction defects to extract more densely packed cellular signals beyond neural spikes. In this regard, we optimize the system performance by developing hybrid point-spread functions (hPSFs) to address the uniformity of the SNR and practical alignment in a customized system, which merge the advantage of both numerical and experimental results, essential for optimum organoid reconstruction.

Achieving these advances, in this work, we introduce a custom-built *hPSF*-FLFM system for fast, volumetric, and high-resolution imaging of entire organoids. In particular, we demonstrate the 3D visualization of the impact of extracellular physical cues on human induced pluripotent stem cells-derived colon organoids (hCOs). The system offers cellular, milliseconds spatiotemporal details of whole-organoid dynamic changes spanning hundreds of micrometers in all three dimensions in instantaneous response to extracellular cues such as osmotic stresses and mechanical forces. We expect the easy adaptability to standard epifluorescence protocols of *hPSF*-FLFM and its cost-efficient scalability to facilitate the approach to the wide variability of organoid model systems. We anticipate the light-field method to provide a promising avenue to explore spatiotemporal-challenging cellular responses in a broad range of organoid research.

2. Material and methods

2.1. Light-field microscope design for organoid imaging

The design of the light-field system for organoid imaging was derived based upon the theoretical model and general design protocol for FLFM (Guo et al., 2019). In particular, a Fourier light-field system consists of optical components in two main categories: *(i)* the components for a standard epifluorescence setup including the objective lens, tube lens, and camera, and *(ii)* the components that generate light-field acquisition, including the Fourier lens (FL) and microlens array (MLA). As a result, designing a FLFM system is to identify the parameters for both the epifluorescence and light-field components to meet the desired imaging performance (Supplementary Note 1).

As detailed in **Supplementary Note 1**, here, in brief, we first determined the epifluorescence components, including a water-dipping physiology objective lens ($\boldsymbol{NA} = 0.80$, $\boldsymbol{M} = 16$), a tube lens ($\boldsymbol{f}_{\mathbf{TL}} = 300$ mm), and a sCMOS camera ($\boldsymbol{P} = 6.5$ μm, $\boldsymbol{D}_{\mathbf{cam}} = 13.3$ mm), where respectively, $\boldsymbol{NA}$ and $\boldsymbol{M}$ represent the numerical aperture and magnification of the objective, $\boldsymbol{f}_{\mathbf{TL}}$ represents the focal length of the tube lens, and $\boldsymbol{P}$ and $\boldsymbol{D}_{\mathbf{cam}}$ represent the camera pixel size and the physical size of the sensor. We then determined the light-field components for organoid acquisition. Specifically, we expect the tissue imaging performance to exhibit sufficient cellular details in all three dimensions and encompass whole-mount organoids without tile acquisition(Dekkers et al., 2019). In this sense, we proposed performance parameters as in a 3D cellular resolution (2–3 μm and 5–6 μm in the lateral x and y and axial z dimensions, respectively) and an imaging volume (>900 μm × 900 μm × 200 μm in x, y, z, respectively). Next, the theoretical model generated a variety of combinatorial performance parameters that meet the expectation (Supplementary Table 1). We selected one such set of performance parameters as $\boldsymbol{R}_{xy} = 3.37$ μm, $\boldsymbol{R}_z = 7.99$ μm, $FOV = 917$ μm, and $DOF = 299$ μm. Lastly, the design parameters for the light-field components can be obtained as $\boldsymbol{f}_{\mathbf{FL}} = 200$ mm, $\boldsymbol{d}_{\mathbf{MLA}} = 1.30$ mm, $N = 3$, $\boldsymbol{f}_{\mathbf{MLA}} = 30$ mm, $\boldsymbol{d}_1 = 3.30$ mm, and $\boldsymbol{d}_{\mathbf{max}} = 4.67$ mm. Notably, the high scalability and design flexibility of light-field systems allow this design protocol to produce any possible combination of elements to address different imaging needs in organoid model systems.

2.2. Experimental setup

On the basis of the design parameters, the imaging system was constructed as an entirely custom-built upright microscope implemented with a 16 × , 0.8 NA, water-dipping physiological objective lens and a blue light-emitting diode (LED) (Fig. 1a and Supplementary Fig. 1). As detailed in Supplementary Methods and Materials, the epifluorescence emission was collected through the customized aperture and dichroic mirror (Supplementary Fig. 1) and distributed equally into a wide-field and a light-field path by a 50:50 beam splitter. In the wide-field path, the native image plane (NIP) was recorded using an sCMOS camera as the ground truth and for comparison. In the light-field path, the epifluorescence NIP was Fourier transformed in conjugation to the aperture plane of the objective lens using a Fourier lens. The back focal plane of the Fourier lens was partitioned by a 3 × 3 customized microlens array (MLA, Supplementary Fig. 1), forming an array of elemental images on its back focal plane, which was recorded by a second sCMOS camera.

2.3. Image formation and hybrid point-spread functions (hPSFs)

Fourier light-field systems realize spatially uniform sampling and parallel image formation and retrieval, which permits a unified 3D PSF in describing the light-field propagation (Fig. 1b and Supplementary Fig. 2) (Cong et al., 2017; Guo et al., 2019). Therefore, the elemental images formed on the camera plane in the light-field path can be considered as the convolution of the object and the 3D PSF, which, an inverse process, underlies the reconstruction of the object space through the deconvolution of the camera image with the 3D PSF. As a result, a 3D PSF to faithfully depict the system determines the reconstruction precision and final image quality, especially essential for tissue imaging that utilizes custom elements and collects signals through a considerable volume depth.

In practice, the 3D PSF can be generated through either experimental or numerical procedures. However, for the experimental PSF, the image quality may be affected due to fluorescence fluctuations and a lowering SNR as the imaging depth increases. In contrast, for the numerical PSF, the reconstruction precision may be worsened due to the actual system misalignment or aberrations. Therefore, both strategies may result in a suboptimal reconstruction performance, which becomes especially detrimental for the proposed system to extract fine cellular details throughout a large imaging volume. In this work, we employed a hPSF strategy for image analysis (detailed in Supplementary Note 2 and Supplementary Fig. 3). In brief, at each axial position, the intensity profile of the PSF was determined by the numerical PSF, and its lateral location was decided by the corresponding experimental results. Here, unlike the previous hPSF solution that only considered the positional deviation at the focal plane (Hua et al., 2021), owing to the custom MLA, the PSF may exhibit inconsistent deviations at varying depths, which requires a hPSF to be derived on each layer (Supplementary Note 2). We generated both the experimental and numerical PSFs under the same condition (e.g., the coverslip, water immersion, etc.). Using this hPSF strategy, the reconstruction process was calibrated for deviations while achieving a consistent high SNR to avoid computational artifacts across the entire imaging depth.

2.4. Organoid preparation and staining

The frozen vial of human iPSC-derived colon organoids (hCOs) was purchased from Millipore Sigma (SCC 300). Organoids were cultured according to the supplier's protocols in general. Briefly, organoid fragments were embedded in 25-μL growth factor reduced Matrigel (GFR MG, Corning 356231) domes (protein concentration 8 mg/mL). After gels solidify in the incubator, 500–750 μL of media were added. For the first 3 days after thawing or passaging, ROCK inhibitor Y-27632 (R&D Systems 1254) were added to the media to prevent cell death. Then

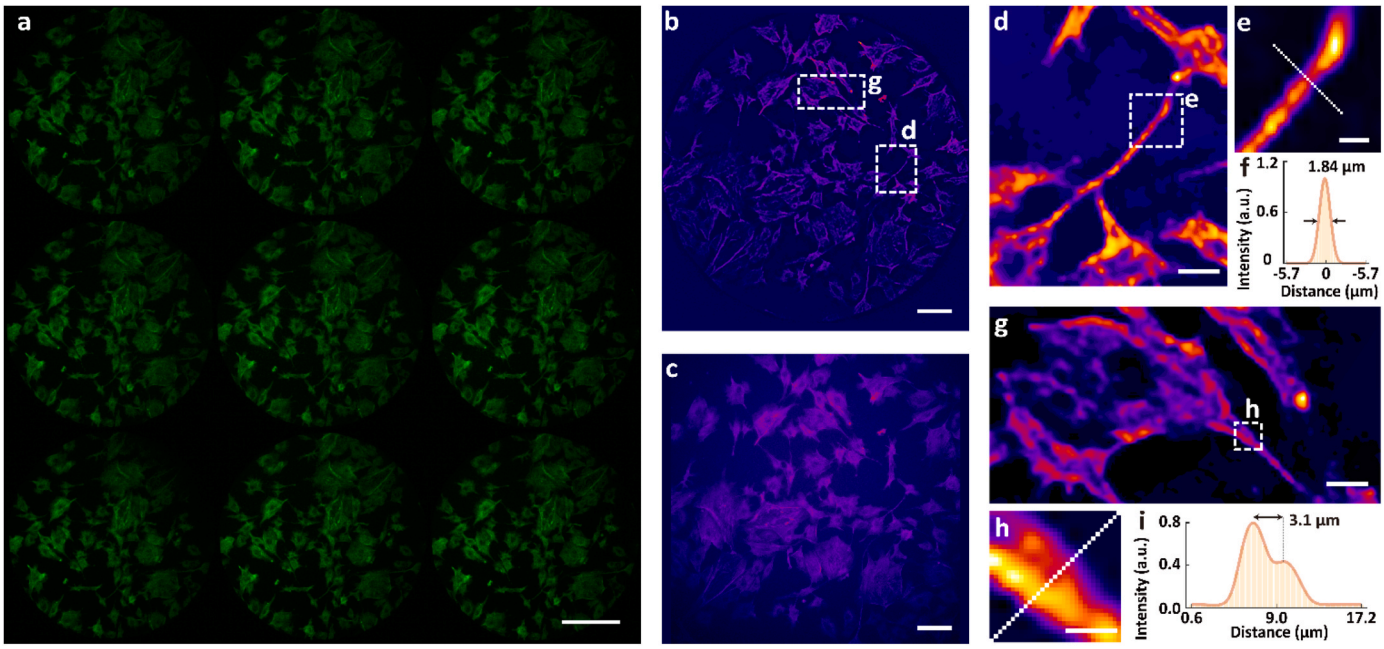

Fig. 2. Imaging bovine pulmonary artery endothelial (BPAE) cells using *hPSF*-FLFM. a,b Raw light-field (a) and 3D reconstructed *hPSF*-FLFM (b) images of immunostained F-actin in BPAE cells taken at an exposure time of 0.1 s c Wide-field image of the same area as in b, showing consistent cellular information at a 6% reduced field of view compared to b. d,g Zoomed-in images of the corresponding boxed regions in b. e,h Zoomed-in images of the corresponding boxed regions d,g. f,i Cross-sectional intensity profiles along the corresponding dashed lines in e,h, respectively, showing well-resolved subcellular filamental structures. Scale bars: 250 μm (a), 100 μm (b, c), 20 μm (d, g), 5 μm (e, h).

media were exchanged every 2 days until the following passage. Organoid culture media components and concentrations are detailed as described in Supplementary Table 2. Organoids used in this work are, in general, at day 5–7 after passaging (Crespo et al., 2017).

Matrigel domes containing the organoids were collected using wide bore P1000 pipet tips. When separating organoids from the gel, scalpels were used, and extra care was taken to maintain the structural integrity of the organoids. After excessive gel was removed, organoids were suspended in wash media (Advanced DMEM/F12 with 15 mM HEPES and GlutaMAX) containing 5 μM of Syto 16 (Thermo Fisher S7578) for nuclei staining. After 30–120 min incubation at 37 °C and 5% CO^2, wash media was carefully removed without disturbing the organoids. Organoids were gently resuspended in GFR MG containing 5 μM of Syto 16, and 10–20 μL of GFR MG containing 1–2 organoids were plated on the imaging chamber. After a brief incubation, the gel construct was covered with wash media with Syto 16 and placed on the microscope stage for imaging.

3. Results

3.1. System characterization using caliber and fixed cell samples

To characterize the performance of the *hPSF*-FLFM system, we first imaged caliber samples and measured the 3D reconstructed images (Fig. 1c and Supplementary Fig. 4), including sector stars (Fig. 1c), a negative USAF target, and mesh grid. The samples were attached to green fluorescent tapes and immersed in water. The reconstructed images were used to determine the FOV (~900 μm × 900 μm), homogeneous magnification (~3.6 ×), and lateral resolution (~2.20 μm) of the system, consistent with our designated performance parameters (Supplementary Note 1).

Next, we imaged 2-μm green fluorescent beads distributed in agarose gel and measured the 3D reconstructed images at varying depths (Fig. 1d and Supplementary Fig. 5). The focal images of the volume were synthesized by the light-field system taken within a single camera frame, consistent with the 232 axial stacks (step size = 400 nm) taken by scanning wide-field microscopy (Fig. 1e). The reconstructed images were Gaussian-fitted and exhibited FWHM values of ~2 μm and ~6 μm in the lateral and axial dimensions, respectively, across the sample thickness of ~100 μm (Fig. 1f and g), consistent with the theoretical prediction (Supplementary Note 1).

Lastly, to demonstrate cell imaging, we recorded the F-actins of bovine pulmonary artery endothelial (BPAE) cells on a cover slide with phalloidin immuno-stained by Alexa Fluor 488 (Fig. 2a). Notably, the reconstructed light-field image showed consistent subcellular details compared to the same region taken by the wide-field path while providing a ~6% increase in the FOV (Fig. 2b and c). The delicate structural variations of actin bundles can be detectable in the synthesized focal stack, showing consistent morphology with the wide-field image (Fig. 2d–i and Supplementary Fig. 6). In particular, the cross-sectional profiles exhibited that actin bundles of 2–3 μm were well resolved in the light-field images (Fig. 2d–i), presenting a lateral resolution consistent with the measurements using the caliber samples (Fig. 1 and Supplementary Fig. 4).

Notably, in the system characterization procedure, we have also validated that for the custom-built system, the hPSFs exhibited a substantial improvement in the reconstruction precision and final image quality of various caliber and biological samples over the corresponding results obtained by experimental or numerical PSFs (Supplementary Fig. 7). Here, the hPSF approach can effectively tackle practical light propagation due to customized elements such as the MLA and information loss or retrieval defects due to the inadequate SNR, permitting the optimum reconstruction of organoid samples.

3.2. System characterization using organoid samples

We next demonstrated Fourier light-field imaging of 5–7 days old human iPSC-derived colonic organoids (hCOs), which were contained in Matrigel and incubated with a nucleic acid stain, Syto16. As seen, the organoids can be visualized exhibiting a wide variety of tissue morphology at this developmental stage (Fig. 3a,f,i and Supplementary Fig. 8). The system recorded the incident light field of each organoid into

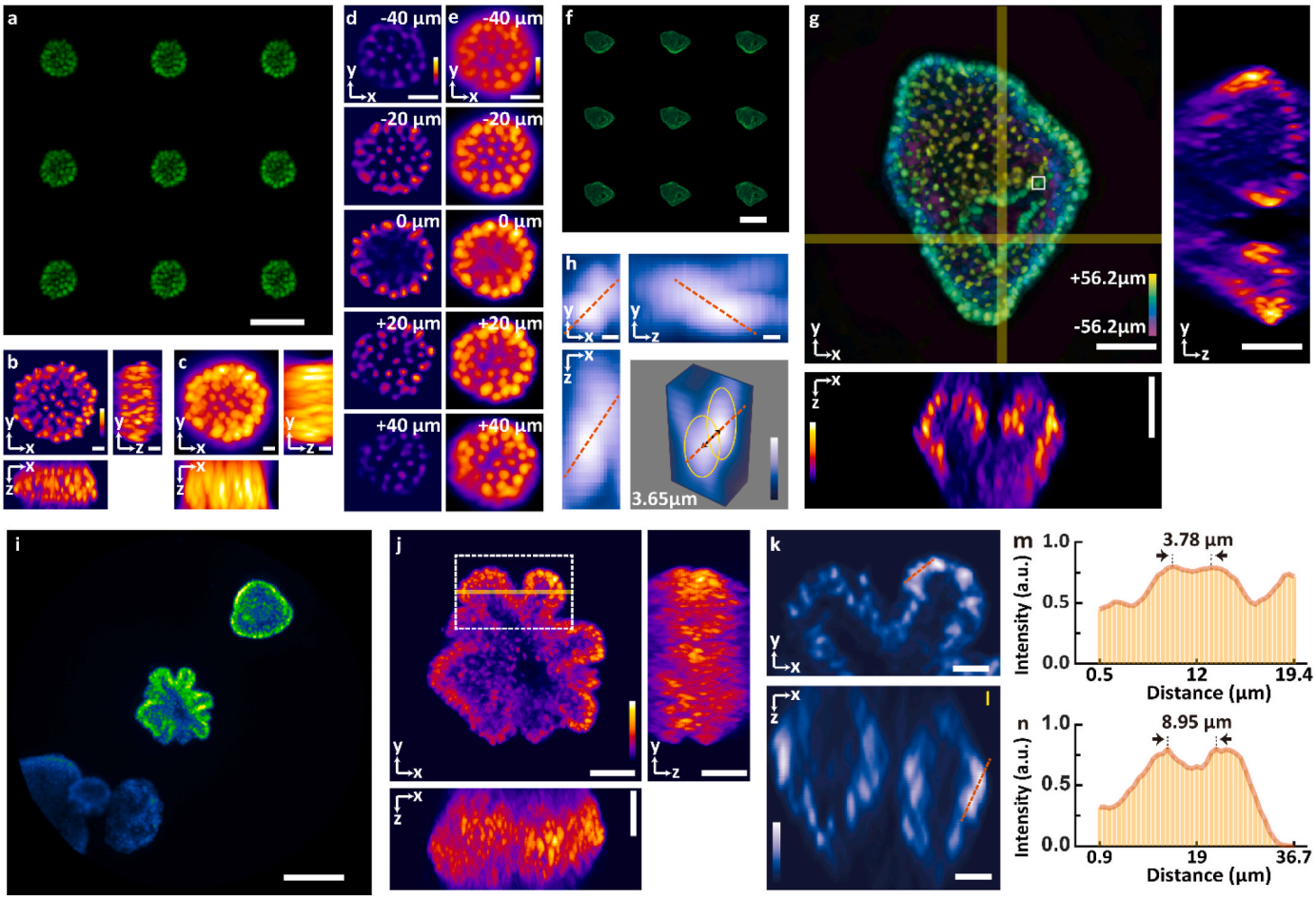

Fig. 3. Imaging organoids using *hPSF*-FLFM. a,b Raw light-field (a) and 3D reconstructed *hPSF*-FLFM (b) images of hCOs stained in nucleus with Syto 16 and taken at an exposure time of 0.1 s c Scanning wide-field MIP images of the same organoid, acquired by overlaying 202 axial stacks at a step size of 400 nm d Synthesized light-field images show consistent cellular structures and enhanced optical sectioning and contrast throughout an 80-µm depth range in comparison with wide-field stack images. f,g Raw light-field (f) and 3D reconstructed *hPSF*-FLFM (g) images exhibiting prominent hollow lumen of hCOs in all three dimensions (insets). h Zoomed-in images of the boxed volume in (g), showing well-resolved 3D individual nucleic structures separated as close as 3.65 µm i Central element of the raw 3 × 3 light-field images of multiple hCOs captured in one camera frame. j 3D reconstructed *hPSF*-FLFM images of a budded organoid. k,l Zoomed-in images of the boxed crypts (k, *x*-*y*) and along the yellow line (l, *x*-*z*) in (j), displaying thin epithelial lining separating the lumen from the outer environment. m,n Cross-sectional profiles along the red dashed lines in k,l, respectively, resolving epithelial cellular structures at a few micrometers in all three dimensions. Scale bars: 100 µm (a), 20 µm (b, c, k, l), 50 µm (d, e, g, j), 2 µm (h), 200 µm (f), 150 µm (i).

nine elemental images, allowing for the reconstruction of the full volume of organoid samples using a single camera frame at a volume acquisition time of 0.1 s. Remarkably, *hPSF*-FLFM is able to recover the nucleic structures in organoids that were out-of-focus and poorly sectioned with axial stacks using wide-field microscopy (Fig. 3b–e and Supplementary Fig. 8). For example, the system clearly resolved the hollow lumen of the organoid in all three dimensions, a prominent feature of hCOs (Fig. 3g). Also, the 3D reconstructed image of two adjacent crypts of a budded organoid displayed the entire thin epithelial lining separating the lumen from the outer environment (Fig. 3j–l). Quantitatively, the high 3D resolution allows us to characterize the organization of individual cellular nuclei in organoids that are separated as close as ~3 µm in all three dimensions (Fig. 3h, m, n). Also, the large imaging volume of the light-field system allows capturing complete and multiple organoids spanning a diameter over hundreds of micrometers without the need for scanning or tile acquisition. Here we are able to screen a large batch of organoids at a fast snapshot rate (primarily determined by the camera speed), which procedure may require minutes to hours per organoid of a comparable volume using confocal or light-sheet microscopy (Dekkers et al., 2019). This improvement exhibits >2-3 orders of magnitude faster in the volumetric acquisition, promising substantial abilities to capture rapid dynamic processes while maintaining minimum phototoxicity per organoid acquisition, as well as for within-batch variability analysis for high throughput drug screening assay (Sachs et al., 2018).

3.3. Observation of hCOs under osmotic stress

Extracellular physical cues such as the osmotic and mechanical stresses dynamically regulate a number of physiological processes that underlie the growth and homeostasis of organoids *in vitro* (Hof et al., 2021; Li et al., 2021; Yang et al., 2021). However, the impact of these extracellular physical cues on organoids remains elusive, because at the microscopic level, the cellular compartments in tissue exhibit remarkable spatiotemporal dynamics and heterogeneity in response to the environmental cues, thus posing a challenge for the instantaneous recording of the processes throughout the organoid volume using conventional imaging methods.

Here, we first demonstrated the light-field observation of hCOs under osmotic stress. For this experiment, 5–7 days old hCOs were embedded in Matrigel and the nucleus stained with Syto16. Hyperosmotic stress was applied while imaging by adding 1 mL pre-warmed (37 °C) NaCl solution to the isotonic culture medium (Supplementary Methods and Materials). Without the need for scanning, *hPSF*-FLFM conducted a

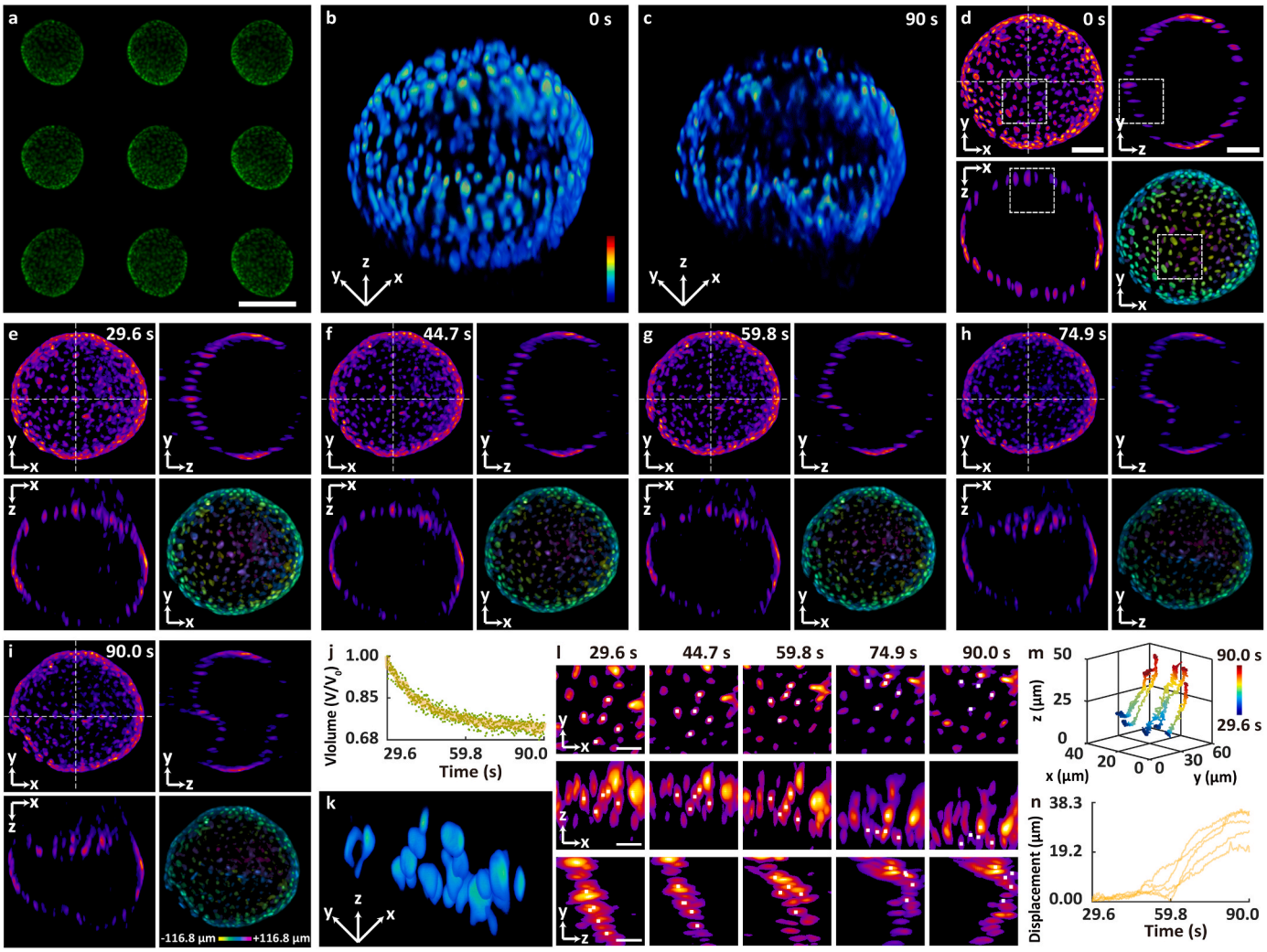

Fig. 4. Observation of organoids under osmotic stress using *hPSF*-FLFM. a,b Raw light-field (a) and 3D reconstructed *hPSF*-FLFM (b) images of a hCO (>200 μm × 200 μm × 200 μm) stained in nucleus with Syto 16 and taken at $t = 0$ s with a volume acquisition time of 10 ms. c Same *hPSF*-FLFM organoid image taken at $t = 90$ s, revealing structural contraction due to osmotic stress. d-i Time-lapse *hPSF*-FLFM images of the organoid at $t = 0$, 29.6, 44.7, 59.8, 74.9, 90.0 s, respectively, displaying *x-y* MIP, *y-z* and *x-z* cross-sectional, depth-coded *x-y* MIP views of the organoid deformation. The depth information is coded as in the color-scale bar in (i). j Volume variation over >1-min period after osmotic stress was induced during $t = 1$–5 s k Volumetric rendering of the boxed region in (d). l *x-y*, *y-z*, and *x-z* views of the volume at time points $t = 0$, 29.6, 44.7, 59.8, 74.9, 90.0 s m 3D trajectories of five cells marked by the white squares in (l). n Corresponding displacements of the five cells over the time period between 29.6 and 90 s, exhibiting an accelerated contraction in this region due to heterogeneous osmotic response. Scale bars: 200 μm (a), 50 μm (d), 20 μm (l).

continuous time-lapse observation of organoids with low wide-field light exposure (<0.6 mJ cm^{-2} per volume acquisition) at a volume acquisition time of 10 ms over tens of thousands of time points without noticeable photodamage (Fig. 4a and Supplementary Fig. 9). Notably, the reconstructed images clearly identified >200 μm-level individual nuclei over the entire sample volume >200 μm × 200 μm × 200 μm within a single camera snapshot, revealing that the cellular architecture is organized across a single-cell layer to form the spherical epithelial lining of the organoid (Fig. 4b and c). As the NaCl solution was introduced gradually from the edge of the Petri dish between $t = 1$–5 s, the entire organoid rapidly reduced under the osmotic pressure as a result of water efflux from the intact organoids. This instant large-scale collective process has been primarily observed only in single cells with conventional imaging methods (Guo et al., 2017) (Fig. 4d–i). As observed, the whole volume underwent instant compression at the beginning, and subsequently, a subregion at the top of the organoid contracted inwards abruptly, indicating the high spatiotemporal heterogeneity of the cellular response to the osmotic stress (Fig. 4d–i and Supplementary Movies 1,2). Over a time period of ~1.5 min, we observed the volume of the hCO was reduced by 32.3% under the hypertonic condition with the 4.52% NaCl solution, compared with that in the original isotonic media (Fig. 4j). Furthermore, the high resolution of *hPSF*-FLFM allows us to characterize the dynamic process under osmotic cues at the single-cell level. In particular, we were able to continuously track the cells in all three dimensions within the most dynamic subregion close to the top of the organoid (Fig. 4k–n). As seen, the cells exhibited moderate motions at the initial stage as a part of the collective volumetric compression and were substantially accelerated to a local structural contraction due to the osmotic stress (Fig. 4n). These results demonstrated the ability of light-field observation of volumetric organoid dynamics without compromising the spatial and temporal resolution. It should also be noted that with multi-color imaging, the spatiotemporal resolution of *hPSF*-FLFM will allow us to characterize individual cell volume changes with richer information, promising the study of extracellular cues in a multiscale manner from the intact organoid to the single-cell levels.

Supplementary video related to this article can be found at https://doi.org/10.1016/j.bios.2022.114201

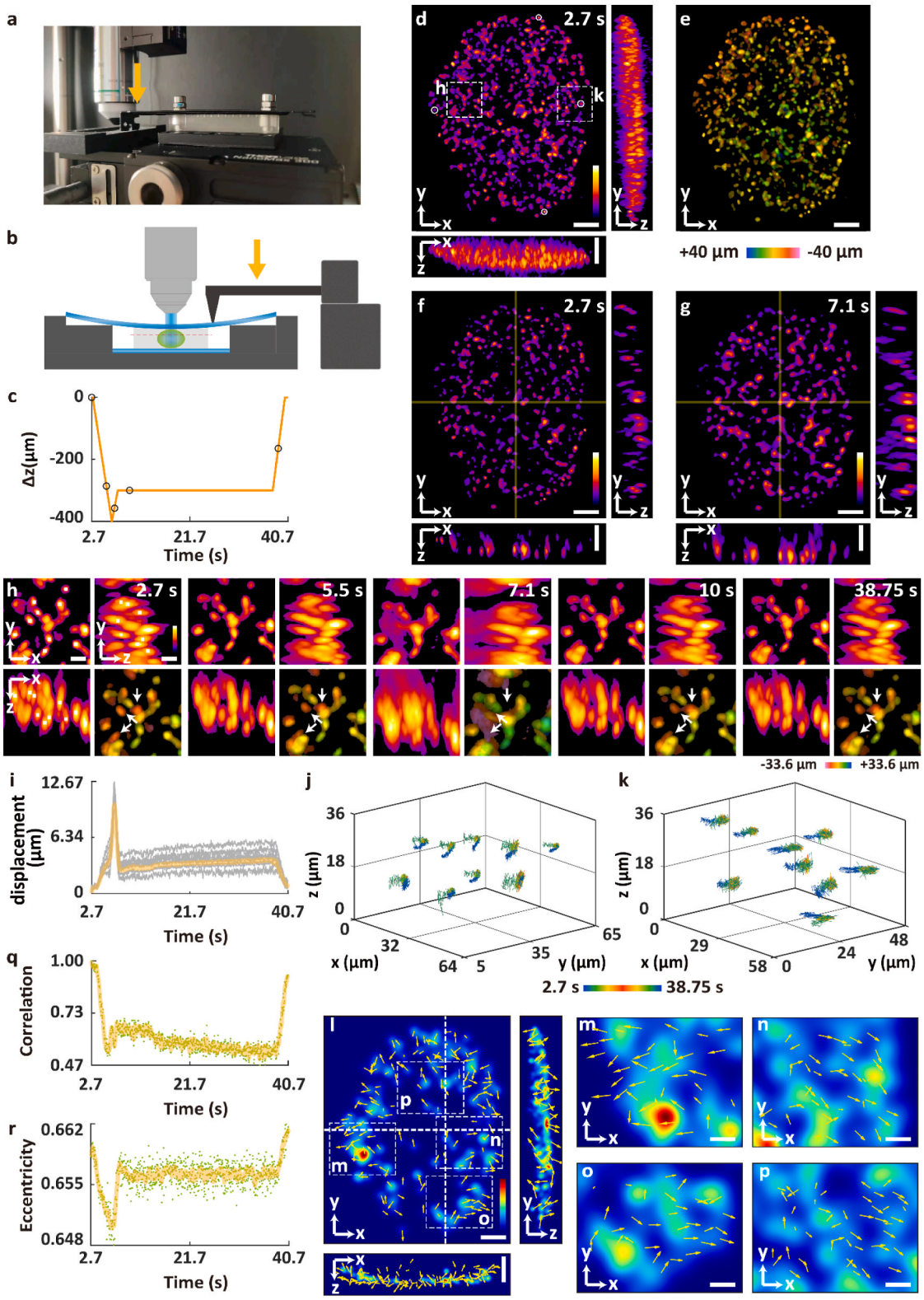

Fig. 5. Observation of organoids under mechanical perturbation using *hPSF*-FLFM. a,b Photo (a) and schematic (b) of the motor-controlled mechanical loading module. c Diagram for mechanical loading and uploading distance by the motor. d,e 3D reconstructed *hPSF*-FLFM (d) and depth-coded (e) MIP images of a hCO at $t =$ 2.7 s f,g Synthesized *hPSF*-FLFM *x-y* focal image at $z = 14.8$ μm and corresponding *x-z* and *y-z* cross-sectional views along the lines at $t = 2.7$ s (f) and 7.1 s (g), exhibiting organoid deformation due to mechanical stress. h Zoomed-in *x-y*, *x-z*, *y-z*, and depth-coded views of the boxed region in (d) at $t = 2.7$, 5.5, 7.1, 10.0, 38.75 s as circled in (c), showing the compression and recovery process of single cells (arrows). i Displacements of representative cells in (h) over time, showing collective responses to mechanical stress (c). j,k 3D trajectories of cells in the corresponding boxed regions in (d), showing opposite motions under mechanical stress. l Heat map of averaged velocity distribution at $t = 5$ s in all three dimensions. m-p Zoomed-in images of corresponding boxed regions in (l), showing heterogeneous lateral movements under mechanical stress. q Morphology correlation measured through MIP images with respect to the starting frame. r Organoid eccentricity over time measured through circled cells in the MIP images in (d). Scale bars: 50 μm (d, e, f, g, l), 12 μm (h), 20 μm (m–p).

3.4. Observation of hCOs under mechanical compression

Next, we demonstrated the light-field observation of mechanical compression of hCOs. To apply a mechanical load, organoids were encapsulated in Matrigel patty and top-covered by a cover glass. A motor-controlled cantilever was placed on the cover glass to introduce a vertical compression with sub-micrometer motor accuracy (Fig. 5a, Supplementary Fig. 10, and Supplementary Methods and Materials). The large working distance of the light-field system allows the accessibility of the force manipulation to real-time image acquisition (Fig. 5a and b and Supplementary Fig. 10). Using this platform, we captured the time-dependent responses of organoids to mechanical forces through a standard loading-unloading experiment (Shen et al., 2019) (Fig. 5c).

During the cycle, the cover glass was first pressed downwards with a constant speed of 200 μm/s until reaching the programmed maximum displacement of 300 μm, where notably, the movement exhibited an intrinsic 100-μm overrun due to the inertial movement of the motor. The cover glass then remained stationary for 30 s to equilibrate to the pressure within the organoid before it was released upwards at the same speed back to its original position. While the thickness of gel was kept at minimum to affix the organoids and to reduce its influence on mechanical deformation of the tissue, it should be mentioned that the embedding gel was also deformed in the same direction under vertical compression by the cover glass, causing an overall displacement of the organoid, which was excluded from the actual tissue deformation in the analysis to display the nuclei displacement solely due to the compression (Supplementary Methods and Materials). The collective behavior was recorded continuously at a volume acquisition time of 10 ms over the entire course of mechanical perturbation and reconstructed using the hPSF (Fig. 5d–g). As seen, the entire organoid sample first deformed quickly upon application of mechanical stress, then achieved an equilibrate deformed state as the compression was kept constant, and elastically recovered close to its original morphology as the stress was relieved (Supplementary Movie 3). Remarkably, even though both the loading and unloading stages were completed within only 1–2 s, and the high spatiotemporal resolution and volumetric ability of the system allowed capture of the entire dynamic processes with well-resolved cellular-level spatial and temporal details, which exhibited correlative behavior among adjacent cells under the loading and unloading stress (Fig. 5h–k and Supplementary Fig. 11). Over the whole organoid, this ability to extract spatiotemporal characterizations of individual cells leads to the 3D mapping of the velocity variations upon mechanical perturbation, which revealed at the microscopic level, a global vertical deformation but highly heterogeneous lateral movements, despite the expected observation of lateral expansion in response to the indentation in some subregions (Fig. 5l–p). To quantify collective behaviors, the morphological correlation of the whole organoid over the entire test indicated instantaneous and elastic deformation, maintenance of mechanical energy, and recovery upon relaxation (Fig. 5q). Furthermore, the quantification of the eccentricity revealed heterogeneous tissue behaviors in the lateral dimension in response to vertical mechanical cues (Fig. 5r). Interestingly, enabled by the high resolution, both the cellular displacements and organoid eccentricity showed a slight viscous response during the indentation, implying the potential dissipation of mechanical energy owing to either the internal microenvironment of the tissue or the elasticity of the embedding gel (Fig. 5i,r).

Supplementary video related to this article can be found at https://doi.org/10.1016/j.bios.2022.114201

4. Discussion and conclusions

In summary, we have demonstrated *hPSF*-FLFM, a light-field microscopy system using hybrid point-spread functions for fast, volumetric, and high-resolution imaging of entire organoids. Unlike conventional 3D organoid microscopy methods, *hPSF*-FLFM offers scanning-free, snapshot recording with a cellular, milliseconds spatiotemporal resolution of near-millimeter-level whole-mount organoids. In particular, we validated that the hPSF strategy enables 3D characterization of cellular dynamic processes of whole organoids in response to rapid extracellular physical cues, including the osmotic and mechanical stresses. The results have overcome the limitation for the instantaneous recording of rapid cellular details throughout the organoid volume using conventional imaging methods. We anticipate the light-field strategy to promise a new avenue for fast and long-term organoid observation with minimum photodamage per volumetric acquisition compared to existing techniques. Furthermore, as the *hPSF*-FLFM system is fully adaptable to standard epifluorescence protocols, the design and instrumentation are cost-efficient and highly scalable. Combining versatile instrumental, biological, and computational strategies (Liu and Jia, 2021; Vizcaino et al., 2021; Wagner et al., 2021; Wang et al., 2021; Wei et al., 2020; Weisenburger and Vaziri, 2018; Xu et al., 2021; Yoon et al., 2020), we expect *hPSF*-FLFM to enable a wide range of quantitative measurements and inspire future imaging innovations for organoid research and stimulate significant insights into organs *in vivo*.

Data availability

The full design documents of the microscope and the datasets generated and analyzed in this study are available from the corresponding author upon request. The design files for the custom elements will be available upon publication at: https://github.com/ShuJiaLab/Organoid_FLFM.

Code availability

The code has been written in MATLAB (MathWorks) and has been tested with version 2020a. The latest version of the software will be available upon publication at: https://github.com/ShuJiaLab/Organoid_FLFM.

Credit authorship contribution statement

Wenhao Liu: Conceptualization, Methodology, Investigation, Instrumentation, Software, Writing – original draft. Ge-Ah R Kim: Methodology, Investigation. Shuichi Takayama: Conceptualization, Supervision, Funding acquisition. Shu Jia: Conceptualization, Supervision, Writing – original draft, Funding acquisition.

Declaration of competing interest

The authors declare that they have no known competing financial interests or personal relationships that could have appeared to influence the work reported in this paper.

Acknowledgements

We acknowledge the support of the National Institutes of Health grants R35GM124846 (to S.J.) and AI116482 (to S.T.) and the National Science Foundation grants EFMA1830941 and 2145235 (to S.J.).

Appendix A. Supplementary data

Supplementary data to this article can be found online at https://doi.org/10.1016/j.bios.2022.114201.

References

Alladin, A., Chaible, L., Garcia Del Valle, L., Sabine, R., Loeschinger, M., Wachsmuth, M., Heriche, J.K., Tischer, C., Jechlinger, M., 2020. Tracking cells in epithelial acini by light sheet microscopy reveals proximity effects in breast cancer initiation. Elife 9.

Almagro, J., Messal, H.A., Zaw Thin, M., van Rheenen, J., Behrens, A., 2021. Tissue clearing to examine tumour complexity in three dimensions. Nat. Rev. Cancer 21 (11), 718–730.
Bolhaqueiro, A.C.F., Ponsioen, B., Bakker, B., Klaasen, S.J., Kucukkose, E., van Jaarsveld, R.H., Vivie, J., Verlaan-Klink, I., Hami, N., Spierings, D.C.J., Sasaki, N., Dutta, D., Boj, S.F., Vries, R.G.J., Lansdorp, P.M., van de Wetering, M., van Oudenaarden, A., Clevers, H., Kranenburg, O., Foijer, F., Snippert, H.J.G., Kops, G., 2019. Ongoing chromosomal instability and karyotype evolution in human colorectal cancer organoids. Nat. Genet. 51 (5), 824–834.
Broutier, L., Mastrogiovanni, G., Verstegen, M.M., Francies, H.E., Gavarro, L.M., Bradshaw, C.R., Allen, G.E., Arnes-Benito, R., Sidorova, O., Gaspersz, M.P., Georgakopoulos, N., Koo, B.K., Dietmann, S., Davies, S.E., Praseedom, R.K., Lieshout, R., Jnm, I.J., Wigmore, S.J., Saeb-Parsy, K., Garnett, M.J., van der Laan, L. J., Huch, M., 2017. Human primary liver cancer-derived organoid cultures for disease modeling and drug screening. Nat. Med. 23 (12), 1424–1435.
Broxton, M., Grosenick, L., Yang, S., Cohen, N., Andalman, A., Deisseroth, K., Levoy, M., 2013. Wave optics theory and 3-D deconvolution for the light field microscope. Opt Express 21 (21), 25418–25439.
Ching, T., Toh, Y.C., Hashimoto, M., Zhang, Y.S., 2021. Bridging the academia-to-industry gap: organ-on-a-chip platforms for safety and toxicology assessment. Trends Pharmacol. Sci. 42 (9), 715–728.
Clevers, H., 2016. Modeling development and disease with organoids. Cell 165 (7), 1586–1597.
Cong, L., Wang, Z., Chai, Y., Hang, W., Shang, C., Yang, W., Bai, L., Du, J., Wang, K., Wen, Q., 2017. Rapid whole brain imaging of neural activity in freely behaving larval zebrafish (Danio rerio). Elife 6, e28158.
Crespo, M., Vilar, E., Tsai, S.Y., Chang, K., Amin, S., Srinivasan, T., Zhang, T., Pipalia, N. H., Chen, H.J., Witherspoon, M., Gordillo, M., Xiang, J.Z., Maxfield, F.R., Lipkin, S., Evans, T., Chen, S., 2017. Colonic organoids derived from human induced pluripotent stem cells for modeling colorectal cancer and drug testing. Nat. Med. 23 (7), 878–884.
Dekkers, J.F., Alieva, M., Wellens, L.M., Ariese, H.C.R., Jamieson, P.R., Vonk, A.M., Amatngalim, G.D., Hu, H., Oost, K.C., Snippert, H.J.G., Beekman, J.M., Wehrens, E. J., Visvader, J.E., Clevers, H., Rios, A.C., 2019. High-resolution 3D imaging of fixed and cleared organoids. Nat. Protoc. 14 (6), 1756–1771.
Drost, J., Clevers, H., 2018. Organoids in cancer research. Nat. Rev. Cancer 18 (7), 407–418.
Drost, J., van Jaarsveld, R.H., Ponsioen, B., Zimberlin, C., van Boxtel, R., Buijs, A., Sachs, N., Overmeer, R.M., Offerhaus, G.J., Begthel, H., Korving, J., van de Wetering, M., Schwank, G., Logtenberg, M., Cuppen, E., Snippert, H.J., Medema, J. P., Kops, G.J., Clevers, H., 2015. Sequential cancer mutations in cultured human intestinal stem cells. Nature 521 (7550), 43–47.
Fan, J.T., Suo, J.L., Wu, J.M., Xie, H., Shen, Y.B., Chen, F., Wang, G.J., Cao, L.C., Jin, G. F., He, Q.S., Li, T.F., Luan, G.M., Kong, L.J., Zheng, Z.R., Dai, Q.H., 2019. Video-rate imaging of biological dynamics at centimetre scale and micrometre resolution. Nat. Photonics 13 (11), 809.
Grassi, L., Alfonsi, R., Francescangeli, F., Signore, M., De Angelis, M.L., Addario, A., Costantini, M., Flex, E., Ciolfi, A., Pizzi, S., Bruselles, A., Pallocca, M., Simone, G., Haoui, M., Falchi, M., Milella, M., Sentinelli, S., Di Matteo, P., Stellacci, E., Gallucci, M., Muto, G., Tartaglia, M., De Maria, R., Bonci, D., 2019. Organoids as a new model for improving regenerative medicine and cancer personalized therapy in renal diseases. Cell Death Dis. 10 (3), 201.
Guo, C., Liu, W., Hua, X., Li, H., Jia, S., 2019. Fourier light-field microscopy. Opt Express 27 (18), 25573–25594.
Guo, M., Pegoraro, A.F., Mao, A., Zhou, E.H., Arany, P.R., Han, Y., Burnette, D.T., Jensen, M.H., Kasza, K.E., Moore, J.R., Mackintosh, F.C., Fredberg, J.J., Mooney, D. J., Lippincott-Schwartz, J., Weitz, D.A., 2017. Cell volume change through water efflux impacts cell stiffness and stem cell fate. Proc. Natl. Acad. Sci. U. S. A. 114 (41), E8618–E8627.
Hof, L., Moreth, T., Koch, M., Liebisch, T., Kurtz, M., Tarnick, J., Lissek, S.M., Verstegen, M.M.A., van der Laan, L.J.W., Huch, M., Matthaus, F., Stelzer, E.H.K., Pampaloni, F., 2021. Long-term live imaging and multiscale analysis identify heterogeneity and core principles of epithelial organoid morphogenesis. BMC Biol. 19 (1), 37.
Hua, X., Liu, W., Jia, S., 2021. High-resolution Fourier light-field microscopy for volumetric multi-color live-cell imaging. Optica 8 (5), 614–620.
Javidi, B., Carnicer, A., Arai, J., Fujii, T., Hua, H., Liao, H., Martinez-Corral, M., Pla, F., Stern, A., Waller, L., Wang, Q.H., Wetzstein, G., Yamaguchi, M., Yamamoto, H., 2020. Roadmap on 3D integral imaging: sensing, processing, and display. Opt Express 28 (22), 32266–32293.
Kim, J., Koo, B.K., Knoblich, J.A., 2020. Human organoids: model systems for human biology and medicine. Nat. Rev. Mol. Cell Biol. 21 (10), 571–584.
Kratochvil, M.J., Seymour, A.J., Li, T.L., Pasca, S.P., Kuo, C.J., Heilshorn, S.C., 2019. Engineered materials for organoid systems. Nat. Rev. Mater. 4 (9), 606–622.
Laissue, P.P., Alghamdi, R.A., Tomancak, P., Reynaud, E.G., Shroff, H., 2017. Assessing phototoxicity in live fluorescence imaging. Nat. Methods 14 (7), 657–661.
Lancaster, M.A., Knoblich, J.A., 2014. Organogenesis in a dish: modeling development and disease using organoid technologies. Science 345 (6194), 1247125.
Levoy, M., Ng, R., Adams, A., Footer, M., Horowitz, M., 2006. Light field microscopy. ACM SIGGRAPH 2006 Papers 924–934.
Levoy, M., Zhang, Z., McDowall, I., 2009. Recording and controlling the 4D light field in a microscope using microlens arrays. J. Microsc. 235 (2), 144–162.
Li, H., Guo, C., Kim-Holzapfel, D., Li, W., Altshuller, Y., Schroeder, B., Liu, W., Meng, Y., French, J.B., Takamaru, K.I., Frohman, M.A., Jia, S., 2019. Fast, volumetric live-cell imaging using high-resolution light-field microscopy. Biomed. Opt Express 10 (1), 29–49.
Li, Y., Chen, M., Hu, J., Sheng, R., Lin, Q., He, X., Guo, M., 2021. Volumetric compression induces intracellular crowding to control intestinal organoid growth via Wnt/beta-catenin signaling. Cell Stem Cell 28 (1), 63–78 e67.
Liu, W., Jia, S., 2021. wFLFM: enhancing the resolution of Fourier light-field microscopy using a hybrid wide-field image. Appl Phys Express 14 (1).
Llavador, A., Sola-Pikabea, J., Saavedra, G., Javidi, B., Martinez-Corral, M., 2016. Resolution improvements in integral microscopy with Fourier plane recording. Opt Express 24 (18), 20792–20798.
Mu, X., Zhang, Y.S., 2022. Chapter Six - tumor-on-a-chip devices for cancer immunotherapy. In: Amiji, M.M., Milane, L.S. (Eds.), Engineering Technologies and Clinical Translation. Academic Press, pp. 155–195.
Nobauer, T., Skocek, O., Pernia-Andrade, A.J., Weilguny, L., Traub, F.M., Molodtsov, M. I., Vaziri, A., 2017. Video rate volumetric Ca(2+) imaging across cortex using seeded iterative demixing (SID) microscopy. Nat. Methods 14 (8), 811–818.
Osakada, F., Ikeda, H., Sasai, Y., Takahashi, M., 2009. Stepwise differentiation of pluripotent stem cells into retinal cells. Nat. Protoc. 4 (6), 811–824.
Pégard, N.C., Liu, H.-Y., Antipa, N., Gerlock, M., Adesnik, H., Waller, L., 2016. Compressive light-field microscopy for 3D neural activity recording. Optica 3 (5), 517–524.
Prevedel, R., Yoon, Y.G., Hoffmann, M., Pak, N., Wetzstein, G., Kato, S., Schrodel, T., Raskar, R., Zimmer, M., Boyden, E.S., Vaziri, A., 2014. Simultaneous whole-animal 3D imaging of neuronal activity using light-field microscopy. Nat. Methods 11 (7), 727–730.
Rakotoson, I., Delhomme, B., Djian, P., Deeg, A., Brunstein, M., Seebacher, C., Uhl, R., Ricard, C., Oheim, M., 2019. Fast 3-D imaging of brain organoids with a new single-objective planar-illumination two-photon microscope. Front. Neuroanat. 13, 77.
Reynaud, E.G., Peychl, J., Huisken, J., Tomancak, P., 2015. Guide to light-sheet microscopy for adventurous biologists. Nat. Methods 12 (1), 30–34.
Rios, A.C., Clevers, H., 2018. Imaging organoids: a bright future ahead. Nat. Methods 15 (1), 24–26.
Rossi, G., Manfrin, A., Lutolf, M.P., 2018. Progress and potential in organoid research. Nat. Rev. Genet. 19 (11), 671–687.
Sachs, N., de Ligt, J., Kopper, O., Gogola, E., Bounova, G., Weeber, F., Balgobind, A.V., Wind, K., Gracanin, A., Begthel, H., Korving, J., van Boxtel, R., Duarte, A.A., Lelieveld, D., van Hoeck, A., Ernst, R.F., Blokzijl, F., Nijman, I.J., Hoogstraat, M., van de Ven, M., Egan, D.A., Zinzalla, V., Moll, J., Boj, S.F., Voest, E.E., Wessels, L., van Diest, P.J., Rottenberg, S., Vries, R.G.J., Cuppen, E., Clevers, H., 2018. A living biobank of breast cancer organoids captures disease heterogeneity. Cell 172 (1–2), 373–386 e310.
Sato, T., Vries, R.G., Snippert, H.J., van de Wetering, M., Barker, N., Stange, D.E., van Es, J.H., Abo, A., Kujala, P., Peters, P.J., Clevers, H., 2009. Single Lgr5 stem cells build crypt-villus structures in vitro without a mesenchymal niche. Nature 459 (7244), 262–265.
Scrofani, G., Sola-Pikabea, J., Llavador, A., Sanchez-Ortiga, E., Barreiro, J.C., Saavedra, G., Garcia-Sucerquia, J., Martinez-Corral, M., 2018. FIMic: design for ultimate 3D-integral microscopy of in-vivo biological samples. Biomed. Opt Express 9 (1), 335–346.
Serra, D., Mayr, U., Boni, A., Lukonin, I., Rempfler, M., Challet Meylan, L., Stadler, M.B., Strnad, P., Papasaikas, P., Vischi, D., Waldt, A., Roma, G., Liberali, P., 2019. Self-organization and symmetry breaking in intestinal organoid development. Nature 569 (7754), 66–72.
Shen, T., Benet, E., Sridhar, S.L., Abadie, J., Piat, E., Vernerey, F.J., 2019. Separating the contributions of zona pellucida and cytoplasm in the viscoelastic response of human oocytes. Acta Biomater. 85, 253–262.
Sims, R.R., Rehman, S.A., Lenz, M.O., Benaissa, S.I., Bruggeman, E., Clark, A., Sanders, E. W., Ponjavic, A., Muresan, L., Lee, S.F., O'Holleran, K., 2020. Single molecule light field microscopy. Optica 7 (9), 1065–1072.
Vizcaino, J.P., Wang, Z., Symvoulidis, P., Favaro, P., Guner-Ataman, B., Boyden, E.S., Lasser, T., 2021. Real-time light field 3D microscopy via sparsity-driven learned deconvolution. In: 2021 IEEE International Conference on Computational Photography (ICCP), pp. 1–11.
Wagner, N., Beuttenmueller, F., Norlin, N., Gierten, J., Boffi, J.C., Wittbrodt, J., Weigert, M., Hufnagel, L., Prevedel, R., Kreshuk, A., 2021. Deep learning-enhanced light-field imaging with continuous validation. Nat. Methods 18 (5), 557–563.
Wagner, N., Norlin, N., Gierten, J., de Medeiros, G., Balazs, B., Wittbrodt, J., Hufnagel, L., Prevedel, R., 2019. Instantaneous isotropic volumetric imaging of fast biological processes. Nat. Methods 16 (6), 497–500.
Wang, Z., Zhu, L., Zhang, H., Li, G., Yi, C., Li, Y., Yang, Y., Ding, Y., Zhen, M., Gao, S., Hsiai, T.K., Fei, P., 2021. Real-time volumetric reconstruction of biological dynamics with light-field microscopy and deep learning. Nat. Methods 18 (5), 551–556.
Weeber, F., Ooft, S.N., Dijkstra, K.K., Voest, E.E., 2017. Tumor organoids as a pre-clinical cancer model for drug discovery. Cell Chem Biol 24 (9), 1092–1100.
Wei, X., Zhuang, L., Li, H., He, C., Wan, H., Hu, N., Wang, P., 2020. Advances in multidimensional cardiac biosensing technologies: from electrophysiology to mechanical motion and contractile force. Small 16 (50), e2005828.
Weisenburger, S., Vaziri, A., 2018. A guide to emerging technologies for large-scale and whole-brain optical imaging of neuronal activity. Annu. Rev. Neurosci. 41 (1), 431–452.
Wu, J., Lu, Z., Jiang, D., Guo, Y., Qiao, H., Zhang, Y., Zhu, T., Cai, Y., Zhang, X., Zhanghao, K., Xie, H., Yan, T., Zhang, G., Li, X., Jiang, Z., Lin, X., Fang, L., Zhou, B., Xi, P., Fan, J., Yu, L., Dai, Q., 2021. Iterative tomography with digital adaptive optics permits hour-long intravital observation of 3D subcellular dynamics at millisecond scale. Cell 184 (12), 3318–3332 e3317.
Xu, D., Fang, J., Zhang, M., Wang, H., Zhang, T., Hang, T., Xie, X., Hu, N., 2021. Synchronized intracellular and extracellular recording of action potentials by three-dimensional nanoroded electroporation. Biosens. Bioelectron. 192, 113501.

Yang, Q., Xue, S.L., Chan, C.J., Rempfler, M., Vischi, D., Maurer-Gutierrez, F., Hiiragi, T., Hannezo, E., Liberali, P., 2021. Cell fate coordinates mechano-osmotic forces in intestinal crypt formation. Nat. Cell Biol. 23 (7), 733–744.
Yoon, Y.G., Wang, Z.G., Pak, N., Park, D., Dai, P.L., Kang, J.S., Suk, H.J., Symvoulidis, P., Guner-Ataman, B., Wang, K., Boyden, E.S., 2020. Sparse decomposition light-field microscopy for high speed imaging of neuronal activity. Optica 7 (10), 1457–1468.
Zhang, Z., Bai, L., Cong, L., Yu, P., Zhang, T., Shi, W., Li, F., Du, J., Wang, K., 2021. Imaging volumetric dynamics at high speed in mouse and zebrafish brain with confocal light field microscopy. Nat. Biotechnol. 39 (1), 74–83.